Constraining the neutron star equation of state through mass and radius measurements

BSc Varpu Ahlberg

MSc thesis
2022

Reviewers:
Prof. Juri Poutanen
Dos. Sergey Tsygankov

DEPARTMENT OF PHYSICS AND ASTRONOMY

UNIVERSITY OF TURKU
Department of Physics and Astronomy

AHLBERG, VARPU: Constraining the neutron star equation of state through mass and radius measurements
MSc Thesis, 29 pages
Astronomy
November 2022

The equation of state of cold dense matter is not well known. The models for cold dense matter can be constrained through the measurement of neutron stars, as they are the densest directly observable objects in the universe. Their mass-radius relation is determined by their equation of state, making it an important observable. This thesis discusses various methods to measure the masses and radii of neutron stars using X-ray observations. A new model for the optical depth of the accretion funnel of accreting neutron stars is presented.

The thermal emission spectrum of neutron stars can be used for mass-radius measurement. The observed flux depends on the distance and the apparent size of the emitting body. Due to relativistic effects, the apparent size is dependent on both the mass and the radius. The biggest uncertainties in this method lie with the difficulty of measuring distance and the modeling of the emission spectrum itself.

Periodic pulsations in the X-ray flux of neutron stars can be similarly utilized. It is caused by one or more hot spots on the neutron star surface created through some source of uneven heating. The pulse profile is affected by several relativistic effects, which gives its shape a dependence on mass and radius. This method is independent of distance, however it contains multiple difficult to measure parameters such as the geometry of emission.

In accreting neutron stars, the pulse profile is affected by the absorption of light through the accreting plasma. The optical depth is dependent on the direction of emission, causing a dip in brightness when the spot is closest to the observer. The effect can be modeled using simple approximations for the density profile and geometry of the accretion flow. This correction is capable of recreating the secondary minimum seen in certain pulse profiles.

Keywords: MSc thesis, neutron stars, equation of state of dense matter, theoretical models.

Contents

1 Introduction

Neutron stars are the densest observable objects in the universe. Their existence was theoretically predicted in the early 1930s and they were first observed in 1967. They are remnants of supernova explosions of massive stars [1]. A general estimate for their mass is ~ 1.4 $M_\odot$ (solar masses), and for their radius ~ 12 km [2]. Their extreme properties make them excellent laboratories for many fields of physics. This thesis will focus on their use in the study of the cold dense matter equation of state.

Neutron stars can be categorized into several different types. Radio pulsars, or rotation powered pulsars, are rapidly rotating neutron stars exhibiting periodic radio emission. They were the first type of neutron star observed thanks to their characteristic pulsation. Magnetars are strongly magnetic young neutron stars, the emission of which is believed to be caused by the decay of their magnetic fields. They are known to undergo strong outbursts. The drag created by the magnetic fields of rotation powered pulsars and magnetars causes their spin rates to decrease over time [3].

Accretion powered pulsars, such as X-ray pulsars, are neutron stars in binary systems that accrete gas from their companion. This process releases a large amount of energy as X-ray and gamma ray radiation, and it increases their spin rate over time. So-called recycled pulsars are radio pulsars with an especially high spin rate caused by a past period of accretion [4].

The inner structure of neutron stars is not well known. Most of their mass is situated in their core, the density of which is believed to be 5-10 times the nuclear saturation density $\rho_0 \sim 2.8 \times 10^{14}$ g/cm^3. The equation of state (EoS) of such cold dense matter remains an unsolved problem. The extremes of such matter has not been possible to create under laboratory conditions, but neutron stars can be used as natural laboratories to probe the EoS [5].

Theoretical modeling of cold dense matter is a complex problem that involves many body interactions in quantum chromodynamics (QCD). The EoS can be experimentally probed at around nuclear saturation density using heavy ion colliders, which gives limits for the EoS at lower densities. The results of such experiments are still model dependent, but they can be used to rule out certain EoS models [5].

Under extreme densities matter might exist in exotic phases such as quark-gluon plasma or strange matter. Due to their complexity, the predictions given by different EoS models vary greatly [6].

The hydrostatic equilibrium of neutron stars follows the Tolman-Oppenheimer-Volkoff (TOV) equation:

$$\frac{\mathrm{d}p}{\mathrm{d}r} = -\frac{G}{c^2}\frac{(p+\epsilon)(m+4\pi r^3 p/c^2)}{r^2[1-2Gm/(rc^2)]}, \tag{1}$$

$$\frac{\mathrm{d}m}{\mathrm{d}r} = 4\pi r^2 \frac{\epsilon}{c^2}. \tag{2}$$

Importantly, the EoS defines the pressure-energy relation in the TOV equation. If the mass-radius ($M-R$) relation of neutron stars is measured, the EoS models can be constrained further [7]. Figure 1 shows multiple different EoS models and their corresponding $M-R$ relations [8].

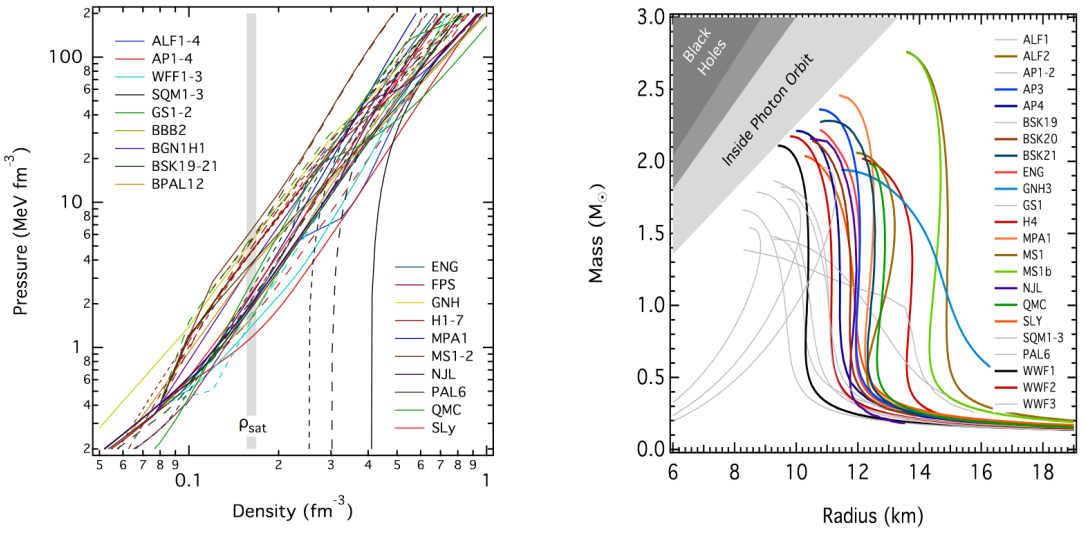

Figure 1: Plots of various models for the equation of state and their corresponding $M - R$ relations.

2 The cold dense matter EoS and its effects on neutron stars

2.1 The internal structure of neutron stars

The structure of neutron stars is important to the cold dense matter EoS. A vast majority of a neutron star's mass is located in its core. The density of the outer core is about $\sim 1-2\rho_0$ and it consists of protons and neutrons in a superfluid state. The inner core is much more dense, with densities even as high as $5-15\rho_0$. The predicted composition of the inner core depends on the EoS model. Some models predict the presence of various exotica such as hyperons and deconfined quarks. Next from the core is the crust, which can be divided into outer and inner parts. The density of the inner crust exceeds the neutron drip density, so the matter becomes increasingly more neutron rich at higher depths through inverse β-decay. The outer crust, which consists of ions and electrons, is followed by a $\sim$ 100 m thick layer known either as the ocean or the envelope. It is the boundary between the isothermal interior and the effective temperature of the visible surface. The atmosphere surrounding the ocean is only a few centimeters thick, and it has a steep temperature gradient. An illustration of this structure is presented in figure 2 [2].

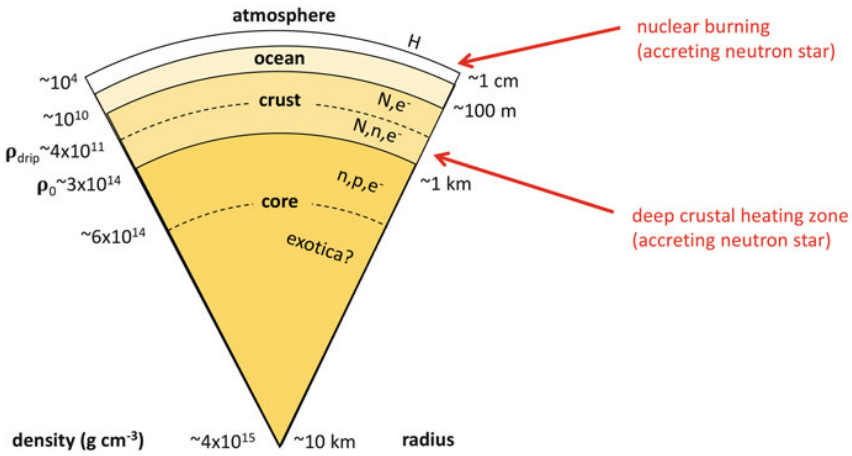

Figure 2: An illustration of the inner structure of neutron stars.

2.2 Limits for neutron stars

The EoS imposes several limits to the physical properties neutron stars. Each model predicts a maximum density, which sets a limit for the maximum stable mass. Models that cannot accommodate observed neutron star masses can be ruled out. Neutron star masses can be accurately measured through pulsar timing, which involves measuring the orbital parameters of neutron stars in binary systems. Millisecond pulsars have an exceptionally stable period, so measuring the time delays of their radio pulses can be used to determine their orbital motion. Pulsar timing has yielded the most accurate mass measurements thus far, and the various factors affecting

the timing model are well understood. The method has been widely used and has resulted in strong EoS constraints [9, 10].

Two mass measurements that have resulted in strong constraints are $M = 2.01 \pm 0.04$ $M_\odot$ for pulsar J0348+0432 [11] and $M = 2.14^{+0.10}_{-0.09}$ $M_\odot$ for pulsar J0740+6620 [12]. Both of them are millisecond pulsars with white dwarf companions. Higher mass neutron stars have been observed, but the observational accuracy has been too low to provide constraints [13, 14].

Secondly, the EoS sets a maximum spin rate for neutron stars. The curve of constant maximum spin rate in the $M - R$ diagram limits the possible masses and radii for neutron stars according to the relation

$$R < 10C^{2/3} \left[\frac{M}{M_\odot}\right]^{1/3} \left[\frac{f}{1 \text{ kHz}}\right]^{-2/3} \text{ km}, \tag{3}$$

where R is the radius of a non-rotating star and C is an EoS dependent constant, the value of which for neutron stars is about 1.08 KHz. If a neutron star is observed to have a spin rate larger than one allowed by an EoS model, that model can be ruled out. However, the highest observed spin rate so far is 716 Hz, which is not high enough to constrain any EoS models [15]. There are two possible reasons why neutron stars with higher spin rates have not been observed: either they are obfuscated by their accretion disks, or there is some process limiting spin rates. There is no known mechanism that makes the discovery of high spin rate neutron stars less likely, but better instrumentation would make finding them easier [16]. Two possible phenomena that could limit the spin rate are the spin-disk interaction and gravitational wave emission. Neither have observational evidence, however [17].

2.3 The tidal deformability limit

In 2017, the first binary neutron star (NS-NS) merger, GW170817, was detected through gravitational waves emitted by the event. When two neutron stars spiral in closer to one another, their orbital period decreases. The accelerating rotation generates gravitational waves, the frequency of which increases over time, which can be seen in figure 3 [18]. Many phenomena affect the increase in frequency, one being the deformation of the merging neutron stars caused by tidal forces. The influence of tidal deformability is fairly small, but it is related to the neutron star EoS. After they collide, the neutron stars merge into a supermassive neutron star, after which it probably collapses into a black hole. Supermassive neutron stars are unstable, and the spectrum of gravitational radiation produced by their oscillations can in principle be connected to the EoS. However, these oscillations are at too high a frequency to be detectable with current instruments [19, 20].

Since only one measurement of neutron star tidal deformability has been made, the possible constraints for the equation of state are limited. To accurately determine the EoS using this method, ~ 10 mergers must be observed. One other NS-NS merger candidate has been observed, GW190425, but it has not resulted in any EoS constraint [21]. Despite the limited data, the upper limit for the binary tidal deformability of GW170817 is one of the strongest EoS constraints. Limiting the

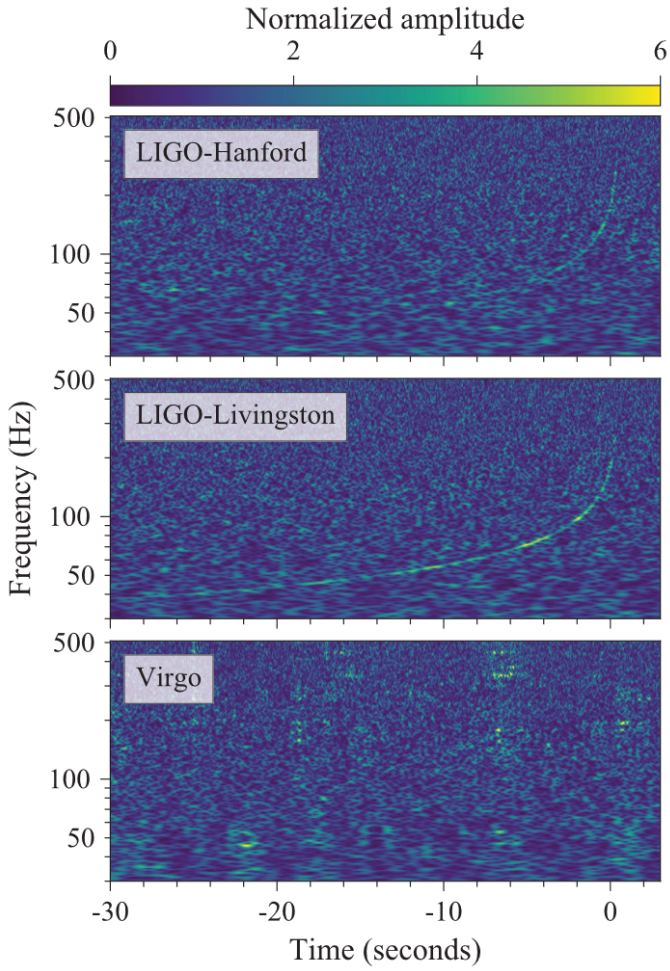

Figure 3: Time resolved gravitational wave spectrum of the NS-NS merger GW170817 measured by several observatories.

lowest maximum mass to ≤ 2 $M_\odot$ narrows the number of possible of EoS models down to about 5×10^5, and adding the deformability limit halves that number [22].

2.4 Challenges in modeling the EoS

The behaviour of matter at densities present in neutron star cores is described by the many-body nucleon-nucleon interaction. The two-body nucleon-nucleon potential is incredibly complicated and depends on many parameters, and expanding it to many-body interactions is everything but trivial. There are two main approaches to model the potential, Ab-initio and phenomenological models. The former begin from a realistic model for the two-body interaction and expand it to calculate the EoS. Phenomenological models on the other hand attempt to replicate the properties of nuclear matter through a number of parameters. As there are multiple ways to approach the problem, there are a huge number of possible EoS models [5].

One problem that neutron star EoS models have is the predicted presence of hyperons. Under conservative assumptions, the forces involving hyperons soften the

EoS so much that the maximum mass of neutron stars would be well below the observed limit. To solve this hyperon puzzle, either some additional repulsive force must be present, or some mechanism reduces the amount of hyperons at neutrons star densities. Similar problems exist with other exotica, like with the presence of dibaryons and Δ isobars. Certain models explicitly allow for the presence of deconfined quark-gluon plasma. This would imply a phase transition occurs, however as it has not been observed, the effect might be weak or simply not present [6].

3 Constraining the neutron star *M-R* relation with X-ray observations

3.1 Spectrum fitting

The observed flux of a star depends on several factors. In an ideal case, it is only affected by the star's distance to the observer, its effective temperature, and the visible emitting area. Therefore, it is possible to measure the radius of a star if its thermal emission spectrum and distance are known. This method can in principle be applied to measure the radius of a neutron star through its thermal emission. However, this proves difficult due to the complexity of the neutron star spectrum and the often difficult to measure distance. A rather important factor in the observed flux of neutron stars is their strong gravity, as it makes relativistic light bending relevant, which makes the flux mass dependent. Thus, by modeling the spectrum of neutron stars and fitting it to observations, a simultaneous measurement forth both mass and radius can be obtained [23].

The mass dependence of the observed flux stems from gravitational lensing of the emitted photons under the neutron star's own gravity. The light emitted from the other side of the neutron star becomes visible as a result of this bending, making the perceived radius larger. Therefore, a correction that takes this into account has to be added to the observed radius. Additionally, the rapid rotation of neutron stars can give them an oblate shape, which has to be taken into account at high spin rates. For extremely high spin rates the light bending is best represented by a Kerr metric, which has to be solved numerically [24]. For an ideal non-rotating, homogeneously emitting neutron star, the observed flux density is

$$F_\nu = \mathcal{F}_{\nu,\infty}\frac{R_\infty^2}{D^2} = \frac{\mathcal{F}_{\nu,(1+z)}}{1+z}\frac{R^2}{D^2}, \tag{4}$$

$$1+z = (1-2GM/c^2R)^{-1/2}, \tag{5}$$

where F_ν is the observed spectral flux density, R_∞^2 the observed radius at infinite distance, and $\mathcal{F}_\nu$ the emitted spectral flux density. The thermal emission spectrum of neutron stars does not usually resemble a perfect black body, as the energy dependence of scattering leads to high-energy photons being generated deeper in the atmosphere. However, the total thermal flux depends on effective temperature according to Stefan-Boltzmann's law. A model spectrum fit can be used to measure the effective temperature, through which equation (4) takes the form [25]

$$F_\infty = \sigma_{\mathrm{SB}} T_{\mathrm{eff},\infty}\frac{R_\infty^2}{D^2},$$

$$T_{\mathrm{eff},\infty} = \frac{T_{\mathrm{eff}}}{1+z},$$

where σ_{SB} is the Stefan-Boltzmann constant.

3.1.1 Neutron star surface emission spectrum

There are two major factors that differentiate neutron star spectra from the Planck spectrum: the extremely strong magnetic field and surface gravity. Bound-free and free-free absorption are highly energy dependent and quickly drop off as energy increases. As a result, high energy photons are emitted from a larger depth where the temperature is higher. This significantly widens and hardens the spectrum when compared to the Planck spectrum at the same effective temperature. At high magnetic field strengths, the bound-free and free-free absorption become weaker and the spectrum becomes softer. Fitting a Planck spectrum to a neutron star spectrum results in a significantly over- or underestimated effective temperature, therefore modeling the radiative transfer through the atmosphere is very important [26].

Because the atmosphere is very thin, a plain-parallel approximation is sufficient for the atmospheric model. It can be modeled as a layer of gas that is heated from below. Assuming hydrostatic equilibrium and local thermodynamic equilibrium, the only factors determining the emergent flux are the atmospheric composition, surface gravity, the effective temperature, and the magnetic field strength. At low temperatures Thomson scattering dominates, and at high temperatures, such as during outbursts, Compton scattering becomes important. Depending on the level of ionization and the atmospheric composition, various spectral absorption features may be present. At low effective temperatures, heavier elements are only partially ionized, making their absorption features more apparent due to photoionization. The magnetic field becomes important if the electron cyclotron energy is significantly larger than the thermal energy. The magnetic field can split and widen spectral lines, and cyclotron absorption features may become visible. Additionally, strong magnetic fields create an anisotropy in the surface temperature, which can make the neutron star unsuitable for spectral fitting [27].

The most uncertain parameter in spectrum modeling is the atmospheric composition. The surface gravity separates the various elements comprising the atmosphere into separate layers unless convection or accretion is present. At the lowest levels of the atmosphere the electrons are in a degenerate state, but this happens at such a depth that it is irrelevant for virtually all models. Because convection only becomes significant at temperatures near the peak of X-ray bursts, non-accreting neutron stars are assumed to have an atmosphere consisting purely of light elements. In accreting neutron stars, if the rate of accretion is faster than the time scale of gravitational separation, the atmosphere has the same composition as the infalling gas. This critical accretion rate is not achieved during periods of quiescence. It is also possible for the atmosphere to consist of heavier elements. For example, carbon atmospheres are not fully ionized and the emergent spectrum is much harder as a result [25]. Figure 4 shows an example of a theoretical model for the spectrum of a hot metallic atmosphere [27].

3.1.2 Spectral line fitting

It has been suggested that it would be possible to detect redshifted spectral lines from the thermal emission of a neutron star. The star's own gravity and spin broaden the spectral lines, so identifying a sufficiently narrow line would allow for $M - R$

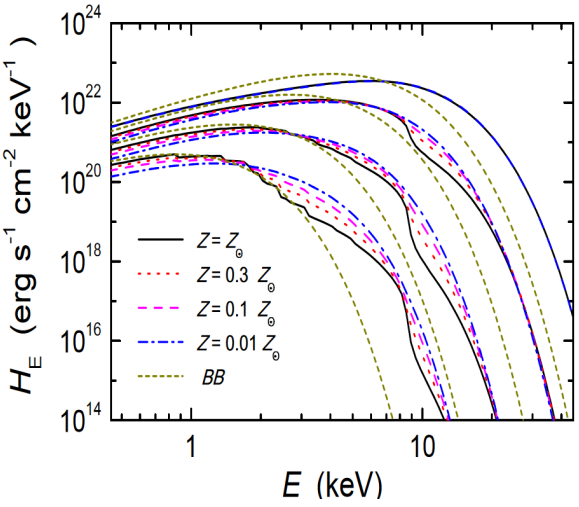

Figure 4: A model for the spectrum of a hot neutron star at different metallicities and temperatures. The green graphs represent the blackbody spectrum at the same temperature.

measurement without many sources of external systematic error. Measuring this broadening of spectral lines can give independent values for both the mass and the radius of the neutron star. In the X-ray region, spectral lines are only detectable in atmospheres where heavy metals are present. In order for the thermal emission to be strong enough to detect spectral lines, the star must also be very hot. Both features suggest that the best candidates for detecting spectral lines are young neutron stars, but their magnetic fields are often strong enough that it causes a large source of systematic error [28].

The conditions for detecting spectral lines should be suitable during X-ray bursts, but the effect of the rapid spin of accreting pulsars may make the spectral lines too wide to be viable for this method. For these reasons, spectral lines have not yet been successfully utilized for $M - R$ measurement [29, 30].

3.1.3 Burst spectra

While the surface emission of accreting neutron stars is blocked by the accretion disk, they are still potential targets for spectral fitting during X-ray outbursts. An outburst is created when newly accreted matter undergoes thermonuclear burning in the neutron star's ocean, which significantly increases its luminosity. On the onset of the burst the spectrum rapidly hardens to a maximum, after which it begins to soften in the cooling tail of the burst. During especially powerful bursts, the radiation pressure might grow enough to surpass the Eddington limit, increasing the size of the photosphere. Such photospheric radius expansion (PRE) bursts present multiple opportunities for $M - R$ measurement [31]. The observed flux at the Eddington limit is

$$F_{\rm edd} = \frac{GMc}{\kappa_{\rm e} D^2} \frac{1}{1+z}, \tag{6}$$

$$1 + z = \frac{1}{\sqrt{1 - 2GM/c^2 R}}, \tag{7}$$

where $\kappa_{\rm e}$ is the electron scattering coefficient, and $1 + z$ is the gravitational redshift factor. Due to Compton down-scattering of high energy photons off of cold electrons near the surface of the neutron star, burst spectra at high luminosities resemble diluted blackbody spectra. Such spectra can be approximated with [32]

$$F_{\rm e} \approx \frac{1}{f_{\rm c}^4} B_{\rm E}(f_{\rm c} T_{\rm eff}), \tag{8}$$

where $B_{\rm E}$ is the blackbody spectrum and $f_{\rm c} = T_{\rm bb}/T_{\rm eff}$ the color correction factor. In an ideal case, $M - R$ measurement can be made using the Eddington flux and the apparent size of the neutron star $A \equiv R_\infty({\rm km})/D_{10}$, where $D_{10} = D/10$ kpc. This is done under the assumption that the Eddington limit is reached at the "touchdown" point, which is when the flux reaches its maximum and the apparent radius its minimum [33]. A downside of the touchdown method is that it is not entirely clear when the Eddington limit is reached. However it is widely agreed that it can be assumed to be at the touchdown point with good accuracy [34].

During the cooling tail of the burst, the apparent size of the star is presumed to no longer change. As a result, the spectral evolution is solely dependent on the evolution of the color correction factor $f_{\rm c}$, which is connected to the Eddington luminosity. A fit of the spectral evolution can therefore be used to measure the Eddington luminosity with only a weak dependency on other factors. As it uses the entire burst tail instead of just the touchdown point, the cooling tail method has significant advantages [35]. The distance dependent Eddington flux and apparent size can be connected to the distance independent Eddington temperature:

$$T_{\rm edd,\infty} = \left(\frac{gc}{\sigma_{\rm SB}\kappa_{\rm e}}\right)^{1/4} \frac{1}{1+z} \propto A F_{\rm edd}^{1/4} (A f_{\rm c})^{-4}, \tag{9}$$

$$g = \frac{GM}{R^2}(1+z), \tag{10}$$

where g is the surface gravity of the neutron star. The distance independence of the Eddington temperature is very useful, as it eliminates the large uncertainty often associated with distance. For a neutron star with a known distance, A, $T_{\rm edd,\infty}$ and $F_{\rm edd,\infty}$ can all be used to constrain possible values for the mass and radius [36].

Observed cooling tail spectra from low-mass X-ray binaries appear to fit theoretical models quite well. However, there are several factors that can affect the burst spectrum. Continued accretion during the burst has a large effect on the burst evolution, and the passive cooling assumed by these models occurs most likely during hard spectral states. As a result, bursts during a period of noticeable accretion or a soft spectral state should not be used with this method. Figure 5 shows $M - R$ constraints obtained from multiple hard-state PRE bursts using the cooling tail method, the shape of the confidence interval following the curve of constant $T_{\rm edd}$ [32].

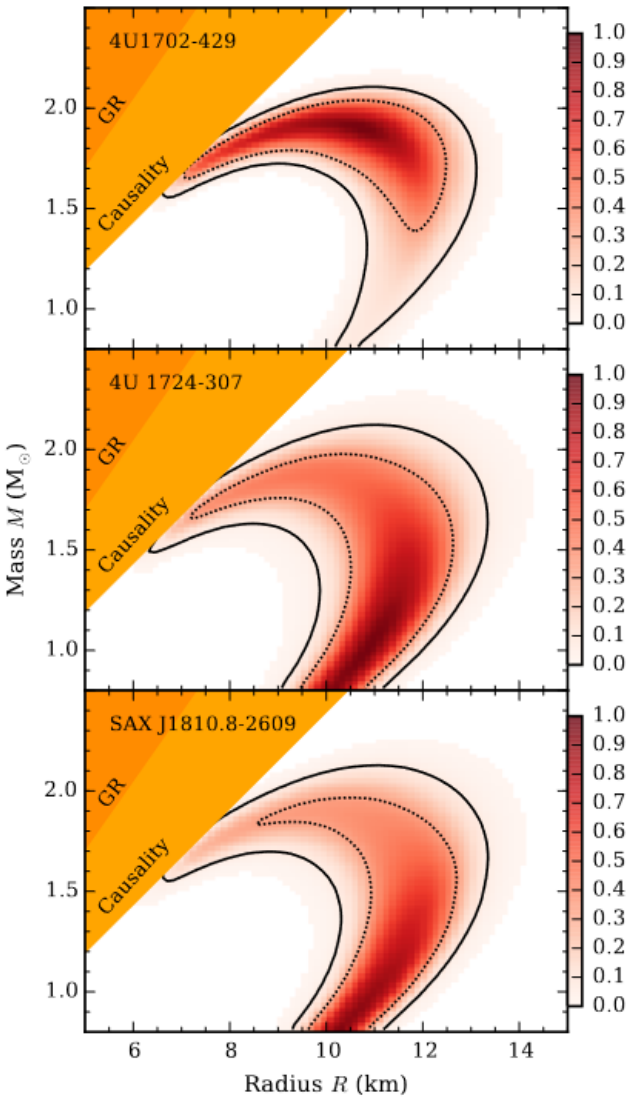

Figure 5: 68 % and 95 % confidence intervals for the mass and radius of multiple neutron stars measured from the cooling tail of hard state PRE bursts. The shape of the interval follows the curve of constant Eddington temperature.

3.1.4 Limitations of spectrum fitting

Not every neutron star is suitable for $M - R$ measurement using X-ray spectrum fitting. Non-thermal emission from accretion disks and magnetic fields obscure the thermal emission, and strong magnetic fields introduce anisotropies that make spectral fitting not viable. The measurement of the surface emission of an accretion powered pulsar is best accomplished during periods of quiescence or during an outburst. The magnetic fields of accretion powered pulsars are expected to be sufficiently weak to not cause issues either [37].

Spectral methods can be used as an EoS probe using the $M - R$ relation. Multiple accurate measurements are required to achieve stringent constraints. The major challenges of this method are the many systematic uncertainties related to the thermal emission spectrum, atmospheric composition, and non-thermal emission of neutron stars. Additionally, external factors such as distance and interstellar extinction are difficult to measure. Errors due to instrument calibration and CCD readout rate are also significant because spectral methods measure absolute flux [38].

Uncertainties related to distance in particular complicate spectral methods. At best, distances can be determined either by parallax or if the target is located in a globular cluster. There are multiple photometric methods commonly used to determine distance to globular clusters, but they contain numerous systematic uncertainties. Geometrical methods such as parallax have a more well defined uncertainty, but it becomes less viable with increasing distance. The relative uncertainty of distance for neutron stars is often as high as $10 - 50\%$ [39]. Overall, the systematic sources of uncertainty in spectral methods are still too large to constrain the Eos with an accuracy of $\leq 5 - 10\%$, but new models and better instruments may achieve the required accuracy in the future.

3.2 Pulse profile modeling

The surface emission of neutron stars is not necessarily homogeneous; certain points on the surface of a neutron star may be hotter than its surroundings. There are multiple processes that create such "hot spots" on the surface. In rotation powered pulsars they are believed to be created by electron-positron pair production in the magnetosphere. When the positrons guided by the field lines collide with the surface, they heat the star's magnetic poles. In accretion powered pulsars, uneven heating occurs when the infalling gas that is frozen in with the magnetic field lines and collides with the magnetic poles. X-ray bursts can also create locally heated areas on the surface of the star.

The rotation of the hot spot relative to the observer creates a noticeable periodic change in the X-ray flux. This pulse profile is not simply sinusoidal, as several relativistic effects, such as Doppler shift, aberration, and light bending distort its shape. These phenomena depend on the mass and radius the neutron star, so a pulse profile model fit can be used for $M - R$ measurement [2].

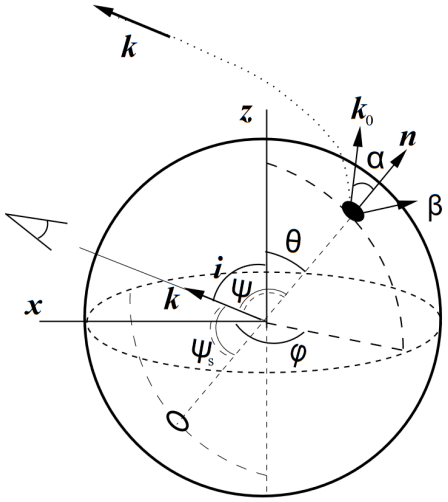

Figure 6: The geometry of emission from a hot spot on the surface of a neutron star. $\boldsymbol{n}$ is the surface normal of the emitting spot, and $\boldsymbol{k}$ is the direction of emission. The dashed curve represents the light bending trajectory.

3.2.1 Relativistic effects on the pulse profile

The shape of the pulse profile is affected by many parameters. One big factor is the geometry of the emitting spot, which is shown in the figure 6. The position of the hot spot relative to the observer changes periodically as the neutron star rotates, which leads to a variability in the apparent surface area and the brightness of the spot. The variability depends on the colatitude of the spot from the axis of rotation θ_0 and the observer inclination i, as well as the shape and size of the spot. The angular dependence of the surface emission must also be taken into account as the observer sees the hot spot from many different angles.

Another important factor influencing the shape of the pulse profile is gravitational light bending caused by the high compactness of neutron stars. The spacetime around a neutron star can be parameterized using the Schwarzschild metric if the effect of rotation is ignored. In the Schwarzschild metric, the light bending can be accurately calculated with [40]

$$\psi(R,\alpha) = \int_R^\infty \frac{\mathrm{d}r}{r^2}\left[\frac{1}{b^2} - \frac{1}{r^2}\left(1 - \frac{R_\mathrm{s}}{r}\right)\right], \tag{11}$$

$$b = \frac{R}{\sqrt{1-u}}\sin\alpha, \tag{12}$$

$$u = \frac{R_\mathrm{s}}{R}, \tag{13}$$

where ψ is the angle between the line of sight and the radial point of emission, α the angle between the initial photon trajectory and the radial point of emission, and R_s the Schwarzschild radius. An accurate analytical approximation for the relation

between the angles is [41]

$$1-\cos\alpha=(1-u)y\left\{1+\frac{u^2y^2}{112}-\frac{e}{100}uy\left[\ln\left(1-\frac{y}{2}\right)+\frac{y}{2}\right]\right\}, \tag{14}$$

$$y=1-\cos\theta, \tag{15}$$

where e is the root of the natural logarithm. Neutron stars rotate so rapidly that relativistic aberration and Doppler shift are also important factors in the pulse profile. The arrival time delays between photons emitted at the same rotational phase also distorts the pulse shape. These factors become relevant at high spin rates, and they give the pulse profile a further radius dependence. Taking everything except time delays into account, the observed flux at distance D is [42]

$$\mathrm{d}F_{\mathrm{E}}=\frac{\sqrt{1-u}}{D^2}\delta^3 I'(E',\alpha')\frac{\mathrm{d}\cos\alpha}{\mathrm{d}\cos\psi}\mathrm{d}S'\cos\alpha', \tag{16}$$

$$\delta=\frac{1}{\gamma(1-\beta\cos\xi)}, \tag{17}$$

$$\gamma=\frac{1}{\sqrt{1-(v/c)^2}}, \tag{18}$$

where I' is the incident radiation spectrum, ξ the angle between the direction of emission and the spot velocity v, and $\mathrm{d}S'\cos\alpha'=\mathrm{d}S\cos\alpha$ the photon beam cross-section [40]. A simulated pulse profile for a rapidly rotating neutron star is shown in Figure 7 [43].

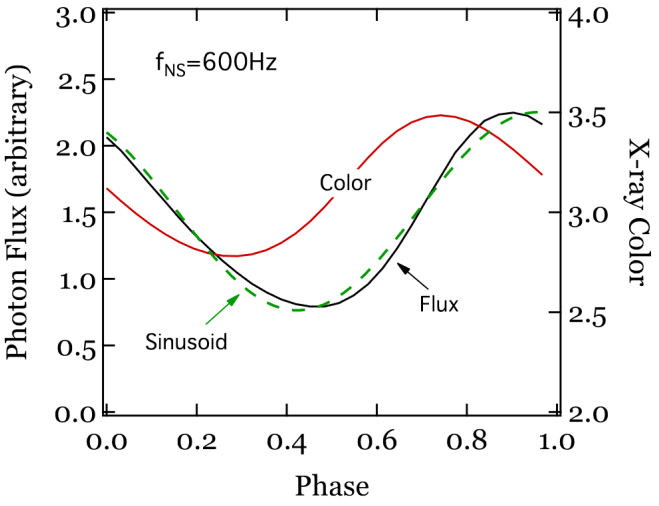

Figure 7: A simulated pulse profile for a neutron star with a spin rate of 600 Hz, showing its deviation from a sinusoidal profile. The change in X-ray color due to Doppler boosting is plotted in red.

3.2.2 Models for the space time metric and the neutron star shape

The various approximations used in the pulse profile model are important in determining its accuracy and the computational power it requires. The Schwarzschild

metric is not truly accurate for rotating objects, as their spin drags the curvature of spacetime. An accurate model for the spacetime around rotating objects is the Kerr metric, which does not have an analytically solvable relation for light bending, and therefore it must be solved numerically. Simulations have shown that the error due to the metric itself is relatively small in the Schwarzschild approximation, with the hitherto observed spin rates and the required measurement accuracy. However, rapidly rotating neutron stars are also flattened at the poles by the centrifugal force, causing significant changes in the pulse profile if its spin frequency is > 300 Hz [44].

Ignoring the oblateness of the neutron star at high spin rates causes a large error, so it should be included in the model for such targets. When deciding what approximations to include for a given model, it is important to consider the requirements for computational power and accuracy. Numerical models using the Kerr metric require considerable computational power; modern computers take up to ten minutes to calculate the pulse profile, while a Schwarzschild metric-based model with a correction for oblateness takes less than a second. The oblate Schwarzschild approximation is commonly used because of this [45, 46].

3.2.3 Hot spot and accretion geometry

Geometric parameters are often challenging to measure and are highly degenerate with the mass and radius, which complicates the process of $M-R$ measurement from pulse profile fits. These include the shape and size of the hot spot, the location of the spot, and the observer inclination. To achieve an accurate $M-R$ measurement, the values of these parameters must somehow be deduced. In many cases, hot spots are assumed to be very small to reduce the number of parameters, as the error stemming from this assumption is almost insignificant for hot spots of size $\leq 45^\circ$ [47].

Numerical magnetohydrodynamical simulations of neutron star accretion have shown various possible hot spot geometries. In the case of disk accretion, the accretion disk becomes disrupted by the magnetic field of the neutron star within the Alfvén radius. The accreting plasma then becomes frozen in with the field lines, guiding it towards the magnetic poles. The hot spots are created as this infalling gas collides with the surface of the neutron star. The dipole moment is often misaligned with the rotational axis, which affects the shape of the hot spot. If the misalignment is small, the hot spot becomes ringlike. At moderate magnetic colatitudes the hot spot takes a crescent shape as gas only flows from one side of the accretion disk. The location of the spot depends largely on the Alfvén and the corotation radius, and its width varies only weakly [48].

3.2.4 Emission models

The beaming pattern of the hot spot is another highly important factor in the modeling of the hot spot as it can mimic the effects of light bending and Doppler boosting. The angular dependency of the surface emission depends on the emission mechanism, but in many cases the process is not well known. The profile of rotation powered pulsars is very stable and the emission pattern is in principle well understood, but there are still uncertainties with regards to the source of the heating.

For accretion powered pulsars, the pulse profile may change within a time scale of days, and their accretion disc can obscure the surface emission. During outbursts, the emission process is well known, but the shape and location of the hot spots are uncertain, and can change at different stages of the burst [49, 50, 51].

In rotation powered millisecond pulsars, the magnetic poles are heated by magnetospheric return currents created through pair production. The depth at which the heating occurs is unknown as it depends on the energy distribution of the infalling particles. Plane parallel atmosphere models show that the radiation pattern is significantly affected by the heating depth. Models that do not take return current heating into account introduce significant error to the beaming pattern as they ignore the heated upper layer of the atmosphere [52].

In accretion powered pulsars, the spectrum resembles a sum of blackbody components at low energies, with a power law component at higher energies. The accreting matter is believed to be stopped by a radiation dominated shock region just above the surface. The surface is heated by the hard x-ray emission of the shock, making it emit like a black body. The shock region acts as a Comptonizing slab, which explains the observed spectra as a result of thermal Comptonization. The power law component may be hardened at high energies by the presence of disk reflection [40, 53].

The polarization of light may help break down the degeneracies related to geometrical parameters. In rotation powered pulsars, the light is expected to be only weakly polarized. For accretion powered pulsars however, the light is scattered by the hot electrons in the accretion shock region, making it strongly polarized. Fits made with simulated data for the Imaging X-ray Polarimetry Explorer (*IXPE*) show much better constraints for the geometrical parameters than what could be previously achieved [54].

3.2.5 Limitations of pulse profile modeling

$M - R$ measurement with pulse profile modeling is applicable to many different targets, making it a versatile method. It does not depend on external factors that are difficult to measure, such as distance, although knowledge of distance can improve accuracy. Pulse profile modeling has been applied to both accretion and rotation powered pulsars. To limit the EoS, several mass and radius measurements with an uncertainty of about $\lesssim 5 - 10\%$ are required, which has only been achieved with pulse profile modeling of millisecond pulsars with the *NICER* X-ray telescope [24, 55]. Although obtaining an independent value for both mass and radius radius with good accuracy can be difficult with this method, measuring the mass through other methods can give a very accurate measurement of the radius [56].

3.3 Quasi-periodic oscillations and astroseismology

Another possible observable for neutron star $M - R$ measurement are quasi-periodic oscillations (QPOs). They are observed in the X-ray flux of accreting neutron stars and black holes. Even though there is no consensus about the underlying process, they are generally believed to be produced in the inner accretion disk. Kilohertz QPOs appear at frequencies that seem to match dynamic processes in the disk, and

therefore might be used to probe the accretion flow. The simplest models connect it to the orbital frequency of infalling matter, but more complex models that predict other QPO modes exist, such as relativistic precession and epicyclic resonance. As these effects depend on the geodesics of the space-time surrounding the neutron star, QPOs can be used to measure neutron star parameters. Thus far the method has only yielded rough mass estimates. In the future, testing the competing models with observations from more accurate instruments might make this a viable method for constraining the EoS [57].

Low-frequency QPOs have also been observed in particularly strong magnetar outbursts. These are believed to be caused by the seismic oscillations generated by the burst, enabling astroseismological study of the structure of neutron stars. From these QPOs it is possible to estimate the propagation speed of the oscillations, which in turn depends on the density, mass and radius of the star. Relativistic effects add an additional dependence on the spacetime metric. However, these models depend on many other factors, making it difficult to constrain the EoS with this method. These include, for example, the Alfvén velocity which depends on the magnetic field, and the composition of the crust and core, which adds effects of superfluidity and superconductivity. Furthermore, the core and crust oscillations are suspected to depend on each other so strongly that they cannot be observationally separated. Strong outbursts that can be used in this purpose are very rare, and QPOs in weaker outbursts are difficult to detect due to their short duration [58].

3.4 Constraints from X-ray observations

The radii of neutron stars have not yet been measured with sufficient accuracy to serve as a good constraint for the EoS. The main reasons for this are systematic uncertainties and the limitations of current instruments [59]. To constrain the equation of state with an accuracy of 10 % three measurements of mass and radius are required with a similar accuracy, and measurements with an accuracy of 5 % would make it possible to differentiate even similar EoS models from one another [56]. The cooling tail method has shown to be capable of measuring radius with good accuracy, but provides weaker constraints for mass unless an EoS is taken as a prior [60].

The only simultaneous $M - R$ measurements with 10 % accuracy so far have been made with pulse profile modeling using the Neutron Star Interior composition explorer (*NICER*). The first *NICER* results were for the millisecond pulsar PSR J0030+045, which has a double-peak pulse profile which hints at several hot spots in the same hemisphere. Two groups made different models for the data, one explaining the geometry with three oval hot spots, the other with one circular hot spot and one crescent-shaped hot spot. The former model measured the mass and radius as $M = 1.44^{+0.15}_{-0.14}$ $\mathrm{M}_\odot$ and $R_{\mathrm{eq}} = 13.02^{+1.24}_{-1.06}$ km [61], and for the latter $M = 1.34^{+0.15}_{-0.16}$ $\mathrm{M}_\odot$ and $R_{\mathrm{eq}} = 12.71^{+1.14}_{-1.19}$ km (68 % confidence level) [62]. As the results are model dependent, they have not resulted in a consensus constraint of the EoS. The model geometries do not fit magnetic dipole models of hot spot formation and therefore multipole models might be needed [63]. Both groups used a non-heated atmosphere model, which might cause significant deviation in the predicted beaming pattern

[52].

The second *NICER* target was the millisecond pulsar PSR J0740+662, the neutron star with the highest accurately measured mass, $M = 2.08 \pm 0.07$ $M_\odot$. The previously measured mass provides a strong prior, however it is much less bright than PSR J0030+045. As with the previous target, the *NICER* collaboration made two separate analyses on the data. Both used models with two circular hot spots, their non-antipodal placement once again hinting at a non-dipole magnetic field. Neither group took the magnetospheric return current heating into account when modeling the beaming pattern, citing that the magnetic field configuration is too unknown and that it would make fits for lower magnetic field strengths less probable. The two radius estimates were $13.7^{+2.6}_{-1.5}$ km (68 % interval) [64] and $12.39^{+2.63}_{-1.68}$ km (95 % interval) [65].

4 Optical depth correction for pulse profiles

Some pulse profiles measured from accretion powered pulsars appear to show a dip at zero phase, which might be caused by the accretion flow dimming the light [66]. Thus far there has been no model accounting for the optical depth of the accretion funnel. In this chapter I will present a simple optical depth correction model that can be applied to pulse profiles. Optical depth can be defined as

$$d\tau = \kappa\rho\, ds, \tag{19}$$

where κ is the opacity, ρ is the density, and ds is the path element. If the accretion region is radiation dominated, the Thomson scattering opacity is a viable approximation. This approximation is valid near the surface for accretion rates of $\gtrsim 10^{-10}$ $\mathrm{M}_\odot$/yr. For significantly lower accretion rates the opacity can be approximated with the Kramer's law, but due to its temperature dependence it is not considered here [67]. If Thomson scattering is used, only the density profile and the light path need to be modeled. The density can be roughly approximated with the continuity equation:

$$\rho(r) = \frac{\dot{M}}{2A(r)v_{\mathrm{ff}}}, \tag{20}$$

where $A(r)$ is the area of the accretion funnel as a function of radius, and $v_{\mathrm{ff}} = \sqrt{2GM/r}$ is the free-fall velocity. For a path parameterized by the angle ψ, the path integral for the optical depth is

$$\tau = \kappa \int_{\psi_{\min}}^{\psi_{\max}} \rho(r(\psi)) \sqrt{\frac{dx}{d\psi}^2 + \frac{dy}{d\psi}^2 + \frac{dz}{d\psi}^2}\, d\psi, \tag{21}$$

where $\psi_{\max}$ and $\psi_{\min}$ are the range of the trajectory.

Using these formula, a rough estimate for the optical depth can be made. Using basic parameters of $M = 1.4$ $\mathrm{M}_\odot$, $R = 12$ km and $\dot{M} = 10^{-10}$ $\mathrm{M}_\odot$/yr, assuming a circular hot spot with an angular radius of $\omega = 15°$, the density of the accretion funnel at the surface is $\rho = 5.8 \times 10^{-7}$ g cm^{-3}. The minimum optical depth from the spot center to the edge is $\tau = 0.07$.

The geometry of the spot and accretion funnel, the emission angle, and the accretion rate are the most important parameters affecting the optical depth. Notably, smaller spot sizes lead to significantly higher optical depths, approximately by $\tau \propto \dot{M}\omega^{-2}$.

4.1 Model for the Light Trajectory

To parameterize the trajectory of the light, let's define two vectors: the direction of the observer, $\boldsymbol{k}$, and the surface normal of the emitting point, $\boldsymbol{n}$. The angle between these two vectors is $\cos\psi_\infty = \boldsymbol{k}\cdot\boldsymbol{n}$. In a coordinate system where the emitting point is aligned with the z-axis, the Cartesian components of the vectors can be written as $\boldsymbol{n}^* = (0, 0, 1)$ and $\boldsymbol{k}^* = (\cos\varphi\sin\psi_\infty, \sin\varphi\sin\psi_\infty, \cos\psi_\infty)$, where φ is the azimuth angle of the emitting direction.

The main parameter of the path is the angle ψ between $\boldsymbol{k}$ and an arbitrary point along the trajectory $\boldsymbol{l}$. For a simple trajectory with no light bending, $r(\psi)$ is solvable from basic trigonometry:

$$r(\psi) = \frac{R\sin(\alpha)}{\sin(\psi)}, \tag{22}$$

where α is the angle between $\boldsymbol{n}$ and the initial direction of emission $\boldsymbol{k_0}$, which in this case is the same as ψ_∞. For light bending, one approximation for the trajectory in the Schwarzschild metric is [68]

$$r(\psi) = \left[\frac{r_\mathrm{g}^2(1-\cos\psi)^2}{4(1+\cos\psi)^2} + \frac{b^2}{\sin^2\psi}\right]^{1/2} - \frac{R_\mathrm{s}(1-\cos\psi)}{2(1+\cos\psi)}, \tag{23}$$

$$b = \frac{R}{\sqrt{1-R_\mathrm{s}/R}}\sin\alpha, \tag{24}$$

$$1-\cos\alpha = (1-\cos\psi_\infty)(1-R_\mathrm{s}/R). \tag{25}$$

This formula is fairly accurate as long as $R > 2R_\mathrm{s}$. Equation (14) is more accurate, however solving $r(\psi)$ with it is not possible analytically. While not correct mathematically, solving α using the more accurate approximation while using equation (23) for the radius might provide somewhat better results. Here, however, I used the less accurate approximation for simplicity.

In the Schwarzschild metric, all points along the light path are on the plane defined by $\boldsymbol{k}$ and $\boldsymbol{l}$. A point along the plane of emission can be expressed in a simple form, $\boldsymbol{l'} = (r\cos\psi, r\sin\psi, 0)$. To calculate $\boldsymbol{l}$ in some other coordinate system, such as one centered on the hot spot, a transform is needed. This can be done using a rotation matrix that turns a point on the plane of emission to the hot spot coordinates where the z-axis is aligned with the spot center. The geometry in the spot center coordinates is shown in figure 8. The general rotation matrices around the three Cartesian axes are

$$\mathbf{r}_\mathrm{x}(\mathcal{X}) = \begin{pmatrix} 1 & 0 & 0 \\ 0 & \cos\mathcal{X} & -\sin\mathcal{X} \\ 0 & \sin\mathcal{X} & \cos\mathcal{X} \end{pmatrix}, \tag{26}$$

$$\mathbf{r}_\mathrm{y}(\mathcal{Y}) = \begin{pmatrix} \cos\mathcal{Y} & 0 & \sin\mathcal{Y} \\ 0 & 1 & 0 \\ -\sin\mathcal{Y} & 0 & \cos\mathcal{Y} \end{pmatrix}, \tag{27}$$

$$\mathbf{r}_\mathrm{z}(\mathcal{Z}) = \begin{pmatrix} \cos\mathcal{Z} & -\sin\mathcal{Z} & 0 \\ \sin\mathcal{Z} & \cos\mathcal{Z} & 0 \\ 0 & 0 & 1 \end{pmatrix}, \tag{28}$$

where $\mathcal{X}$, $\mathcal{Y}$, and $\mathcal{Z}$ are the rotation angles along each of the respective axes. The normal vector of the plane is $\boldsymbol{m} = \frac{\boldsymbol{k}\times\boldsymbol{n}}{\sin\psi_\infty}$. On the plane coordinates, the normal vector $\boldsymbol{m'}$ should be (0, 0, 1), so that $z' = 0$ along the plane:

$$\boldsymbol{m} = \mathbf{r}_\mathrm{x}\mathbf{r}_\mathrm{y}\mathbf{r}_\mathrm{z}\begin{pmatrix} 0 \\ 0 \\ 1 \end{pmatrix} = \begin{pmatrix} \sin\mathcal{Y} \\ -\sin\mathcal{X}\cos\mathcal{Y} \\ \cos\mathcal{X}\cos\mathcal{Y} \end{pmatrix}. \tag{29}$$

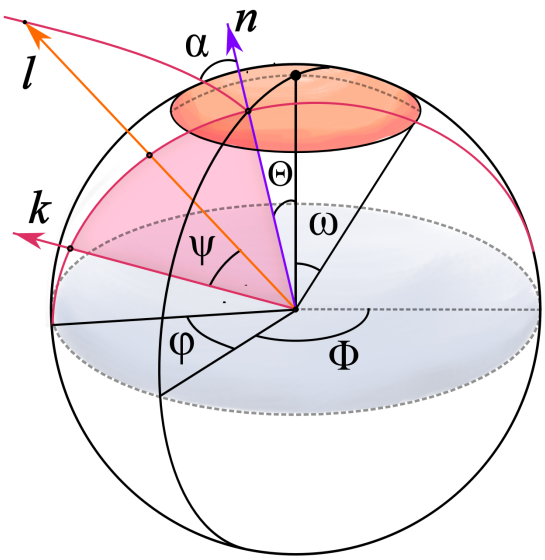

Figure 8: Geometry of the hot spot and the light trajectory in circular coordinates aligned with the spot center. The plane of emission and the trajectory are drawn in magenta, and the circular hot spot is orange.

From this, both $\mathcal{Y}$ and $\mathcal{X}$ can be found. For the third angle, let's define the observer vector $\boldsymbol{k}'$ in the plane coordinates as (1,0,0):

$$\boldsymbol{k} = \mathbf{r}_\mathrm{x}\mathbf{r}_\mathrm{y}\mathbf{r}_\mathrm{z}\begin{pmatrix}1\\0\\0\end{pmatrix} = \begin{pmatrix}\cos\mathcal{Z}\cos\mathcal{Y}\\ \cos\mathcal{X}\sin\mathcal{Z}+\cos\mathcal{Z}\sin\mathcal{Y}\sin\mathcal{X}\\ \sin\mathcal{Z}\sin\mathcal{X}-\cos\mathcal{Z}\sin\mathcal{Y}\cos\mathcal{X}\end{pmatrix}, \tag{30}$$

By combining the rotation angles solved from equations (30) and (29), the full rotation matrix between the plane and spot coordinates can be written as

$$\mathbf{R}_\mathrm{p}(\mathcal{Z},\mathcal{Y},\mathcal{X}) = \mathbf{r}_\mathrm{x}\mathbf{r}_\mathrm{y}\mathbf{r}_\mathrm{z}. \tag{31}$$

With this rotation, a point $\boldsymbol{l}$ along the trajectory in the hot spot coordinates as a function of ψ is

$$\boldsymbol{l} = \mathbf{R}_\mathrm{p}(\mathcal{Z},\mathcal{Y},\mathcal{X})\boldsymbol{l}'(\psi) = \mathbf{R}_\mathrm{p}(\mathcal{Z},\mathcal{Y},\mathcal{X})\begin{pmatrix}r(\psi)\cos\psi\\ r(\psi)\sin\psi\\ 0\end{pmatrix}. \tag{32}$$

The correct angles aren't easy to solve as there are six equations involving trigonometric functions. $\mathcal{Y}$ is the easiest to find using m_x, and a solution for the two others can be found once $\mathcal{Y}$ is known:

$$\mathcal{Y} = \arcsin(m_\mathrm{x}), \tag{33}$$

$$\mathcal{X} = \arccos\left(\frac{m_\mathrm{z}}{\cos\mathcal{Y}}\right) = \arctan\left(\frac{-m_\mathrm{y}}{m_\mathrm{z}}\right), \tag{34}$$

$$\mathcal{Z} = \arccos\left(\frac{k_\mathrm{x}}{\cos\mathcal{Y}}\right). \tag{35}$$

It is important to take sign changes into account, as otherwise these solutions will not work for every possible $\boldsymbol{m}$ and $\boldsymbol{k}$. Firstly, after the y-component of the normal vector reaches zero, the signs of $\boldsymbol{m}$ and the y-component of $\boldsymbol{l}'$ in equation (32) should be flipped, as the direction of the normal vector changes. Secondly, the sign of $\mathcal{Z}$ should be changed after it reaches zero at $k_\mathrm{x} = \cos\mathcal{Y}$.

With this transform, the components of a point along the path now look like $\mathcal{A} \cdot r(\psi)\cos\psi + \mathcal{B} \cdot r(\psi)\sin\psi$, where $\mathcal{A}$ and $\mathcal{B}$ are constants coming from the matrix multiplication in equation (32), which are different for each component. The derivatives of each component have the following form:

$$\mathcal{A}(\dot{r}(\psi)\cos\psi - r(\psi)\sin\psi) + \mathcal{B}(\dot{r}(\psi)\sin\psi + r(\psi)\cos\psi). \tag{36}$$

In order to use ψ_∞ and φ as the parameters that define the direction of emission, another transform is needed. This can be done with a second rotation matrix, one that turns a point centered on the emitting point to the magnetic coordinates. This matrix is

$$\mathbf{R}_\mathrm{m}(\Phi,\Theta) := \mathbf{r}_\mathrm{y} \cdot \mathbf{r}_\mathrm{z} = \begin{pmatrix} \cos\Theta\cos\Phi & -\cos\Theta\sin\Phi & \sin\Theta \\ \sin\Phi & \cos\Phi & 0 \\ -\sin\Theta\cos\Phi & \sin\Theta\sin\Phi & \cos\Theta \end{pmatrix}, \tag{37}$$

where Θ and Φ are the inclination and azimuth angle of the emitting spot from the spot center: $\boldsymbol{n} = (\cos\Phi\sin\Theta, \sin\Phi\sin\Theta, \cos\Theta)$. For a circular spot, the paths as defined by φ and ψ_∞ are symmetric around Φ, and therefore only $\Phi = 0$ needs to be considered. If only Φ is known, φ can be solved using this rotation, as will be discussed later. This rotation can be used to transform vectors $\boldsymbol{k}^*$ and $\boldsymbol{n}^*$ in the emitting spot coordinates to the spot center coordinates. Now, the rotation $\mathbf{R}_\mathrm{p}$ from the plane of emission to the spot center coordinates can be calculated using three parameters: Θ for the location of the emitting spot, and the two angles defining $\boldsymbol{k}^*$, φ and ψ_∞.

For a Cartesian point $\boldsymbol{l}$ along the light path, the inclination in spherical coordinates can be calculated with the conversion $\cos\theta \equiv l_\mathrm{z}/r$. Using equation (32), the inclination of $\boldsymbol{l}$ in spot center coordinates can be written a function of ψ:

$$\cos\theta = \mathrm{R}_{\mathrm{p}31}\cos\psi + \mathrm{R}_{\mathrm{p}32}\sin\psi, \tag{38}$$

$$:= \mathcal{A}_\mathrm{z}\cos\psi + \mathcal{B}_\mathrm{z}\sin\psi, \tag{39}$$

where $\mathrm{R}_{\mathrm{p}31}$ and $\mathrm{R}_{\mathrm{p}32}$ are components of $\mathbf{R}_\mathrm{p}$ at the indicated indices. As the radius term cancels out, the inclination is independent on the shape of the trajectory itself. The maximum inclination for a given trajectory is $\theta_\mathrm{max} = \arccos\mathcal{A}_\mathrm{z}$. By reversing the equation, the angle ψ as a function of θ is

$$\cos\psi = \frac{\mathcal{A}_\mathrm{z}\cos\theta \pm \sqrt{\mathcal{A}_\mathrm{z}^2\mathcal{B}_\mathrm{z}^2 + \mathcal{B}_\mathrm{z}^4 - \mathcal{B}_\mathrm{z}^2\cos^2\theta}}{\mathcal{A}_\mathrm{z}^2 + \mathcal{B}_\mathrm{z}^2}. \tag{40}$$

For a circular spot, one can use similar equations to solve the sign flip thresholds for $\mathcal{Z}$ in equation (33). As mentioned earlier, the sign of $\mathcal{Z}$ should be flipped when

$k_{\rm x} = \cos\mathcal{Y}$. After some algebra the sign flip threshold becomes

$$k_{\rm x} = \mathbf{R}_{\rm m}(0,\Theta)\boldsymbol{k}^*|_{\rm x} = \cos\psi_\infty \sin\Theta + \sin\psi_\infty \cos\Theta\cos\varphi, \tag{41}$$

$$k_{\rm x} = \cos\mathcal{Y} = \sqrt{1-m_{\rm x}^2} = \sqrt{1-\cos^2\Theta\sin^2\varphi}, \tag{42}$$

$$\Rightarrow \psi_\infty > \arccos\frac{\pm\sin\Theta\cos\mathcal{Y}}{\sin^2\Theta+\cos^2\Theta\cos^2\varphi}, \tag{43}$$

where the minus sign corresponds to $\cos\varphi < 0$ and the plus sign to $\cos\varphi > 0$.

4.2 Accretion Column and Hot Spot Geometry

4.2.1 Numerical simulations

As mentioned earlier, 3D numerical simulations of the accretion flow show that for a magnetic pole displacement angle of $\theta_0 \approx 30°$, the shape of the hot spot is a semicircle centered around the magnetic pole. For low displacement angles the hot spot becomes a hollow circle, and for very high inclinations this becomes a bar shape.

For a dipole field, the angle between the center of this spot and the pole is $\theta_{\rm s} = \arcsin\left(\sqrt{\frac{R}{r_{\rm m}}}\cos\theta_0\right)$, where $r_{\rm m}$ is the magnetospheric radius. However, the interaction with the magnetosphere and the disk cause the dipole to be flattened and therefore making this angle smaller. In simulations, the width of this spot is about $7° - 8°$ and only weakly dependent on other parameters [48]. This geometry for the hot spot is not utilized here due to its mathematical complexity, as the trajectory can cross through the accretion funnel twice.

4.2.2 Dipole model

One simpler model for the accretion flow is a circularly symmetric funnel limited by magnetic field lines at the edges. This allows for a parametrization of the optical depth independent of Φ which is a major issue with hollow funnels. As with the previous geometry the trajectory can have multiple crossings, but they happen at higher radii where the density is lower, so they can be neglected. For a perfect dipole, the field lines follow $r = L\sin^2\theta$, where L is the radius at which the field line crosses the equator. Now, the area of the funnel is $A = 2\pi r^2(1-\sqrt{1-\frac{r}{L}})$. The column has no well defined upper edge, so one needs to be defined. It should be smaller than the magnetic radius, which is around a few R for accreting millisecond pulsars. For this purpose, I considered an upper edge of $r_{\rm max} = 3R$. The point of exit for the trajectory is not easily analytically solvable as it is dependent on $r(\psi)$, but is not computationally difficult.

4.2.3 Conical model

To simplify further, the accretion funnel can be modeled as a circular cone with a width of ω. The area of a conical funnel is $A = 2\pi r^2(1-\cos\omega)$. In the dipole model $A \propto r^3$, where as here $A \propto r^2$, which makes this a higher limit for the optical depth compared to the dipole model. As the actual field lines are flattened by the disk

interaction, the accurate area of the funnel is somewhere between the perfect dipole and the cone.

For the conical model, the end point of the trajectory is easily solvable with equation 40 by setting $\theta = \omega$. For a straight trajectory, the optical depth integral becomes $\tau \propto \int d\psi/\sqrt{\sin\psi}$, which has a finite limit at infinite distance. It tends to converge at around $5R$. Limiting the upper edge to $r_{\max} = 3R$ has a significant effect on the maximum optical depth, but it represents the observed disk inner radii better.

4.3 Parameter lookup table of optical depths

I generated parameter lookup tables for the optical depth using the above equations for different hot spot sizes. The accretion rate was fixed at $\dot{M} = 10^{-10}$ $\mathrm{M}_\odot$/yr, and it can be easily changed by scaling the optical depth with a factor of $\dot{M}_{10}$ (accretion rate in units of 10^{-10} $\mathrm{M}_\odot$/yr). The mass and radius of the neutron star were set at $M = 1.4$ $\mathrm{M}_\odot$ and $R = 12$ km. For a spot of radius $\omega = 10°$, the range of optical depths is about 0.1-0.5, with the maximum corresponding to angles at which the light exits through the top edge. Plots for the optical depth as a function of α at fixed φ at spot radii ω of 30°, 15°, and 10° are presented in figure 9.

Most pulse profile models use small spot sizes of $\omega \lesssim 5°$ as it has only a weak effect on the profile, but it strongly effects the optical depth. For small spots, the density is dependent on the spot size approximately by $\rho \propto \omega^{-2}$, which leads to significantly larger optical depths despite the shorter travel distances. Significantly shorter $r_{\max}$ decreases the maximum optical depth, making the distribution over α flatter overall.

To utilize these lookup tables for pulse profiles, the angle φ and Θ need to be found for each emitting spot as a function of rotational phase. The angles ψ_∞ and α are often already calculated, but finding the other two angles usually requires coordinate transforms. A commonly used coordinate system is one centered on the axis of rotation where the observer vector $\boldsymbol{k}'' = (\sin i, 0, \cos i)$ is fixed. Rotating the vectors $\boldsymbol{n}''$ and $\boldsymbol{k}''$ by the rotational phase ϕ and the spot colatitude θ_0 using the matrix $\mathbf{R}_{\mathrm{m}}(-\phi, -\theta_0)$ gives them in the spot center coordinates, where Θ and Φ can be found. φ can be found by further rotating $\boldsymbol{k}$ to the emitting spot coordinates, which can be done with $\mathbf{R}_{\mathrm{m}}(-\Phi, -\Theta)$.

4.4 Pulse profiles

I generated various pulse profiles using the model described in Salmi et al. 2020 [54]. The optical depth correction was applied to each of the emitting points separately to account for time delays. The profiles were corrected for oblation at a spin rate of 401 Hz, and the beaming pattern was calculated using a simple Thomson scattering plane-parallel model described in Viironen & Poutanen 2004 [69]. The corrected profiles are presented in figures 10, 11 and 12 at different accretion rates, spot sizes, and spot colatitudes at an energy of 10 keV. As predicted, the absorption caused by the accretion funnel does indeed cause a periodic dip in brightness at zero phase. The dip remains at the same phase even when the peak is skewed from relativistic

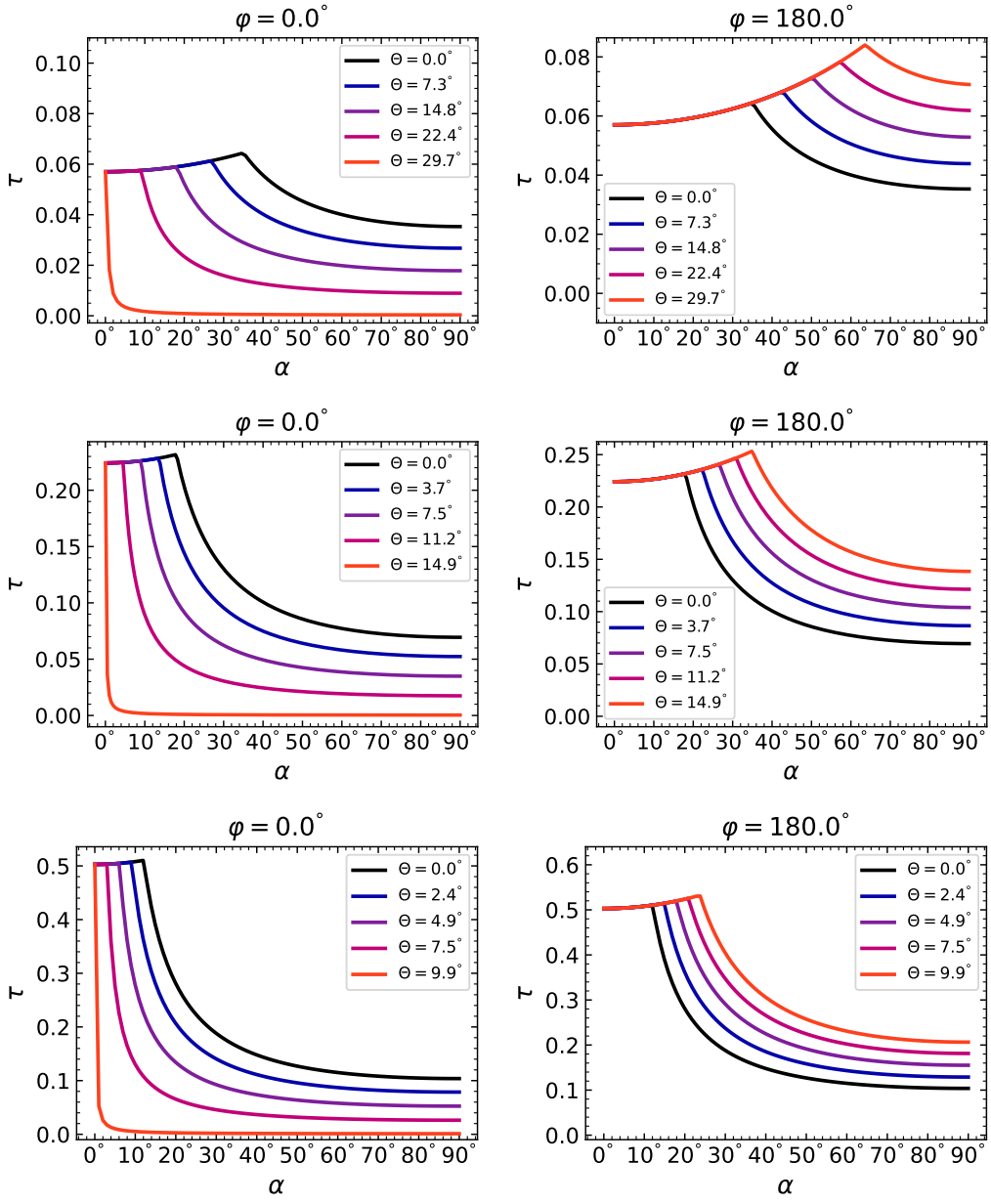

Figure 9: Optical depth of a conical accretion funnel as a function of emission angle α at a fixed azimuth angle φ and inclination Θ for three different spot sizes at $\dot{M}_{10} = 1$. The spot angular radii ω in these plots are $30°, 15°$ and $10°$ (top, center, and bottom plots, respectively).

effects, causing the dip to appear after the peak. The dip is further away from the peak at higher energies.

When the observer inclination is closer to the spot colatitude, the optical depth rises sharply and the dip becomes much more prominent. When $|i - \theta_0| < \omega$ some of the light exits through the upper boundary, which gives the dip a sharper shape. The size of the hot spot affects the depth of the dip, but only weakly changes its width.

The effect of a smaller spot size and a larger accretion rate appear to be quite

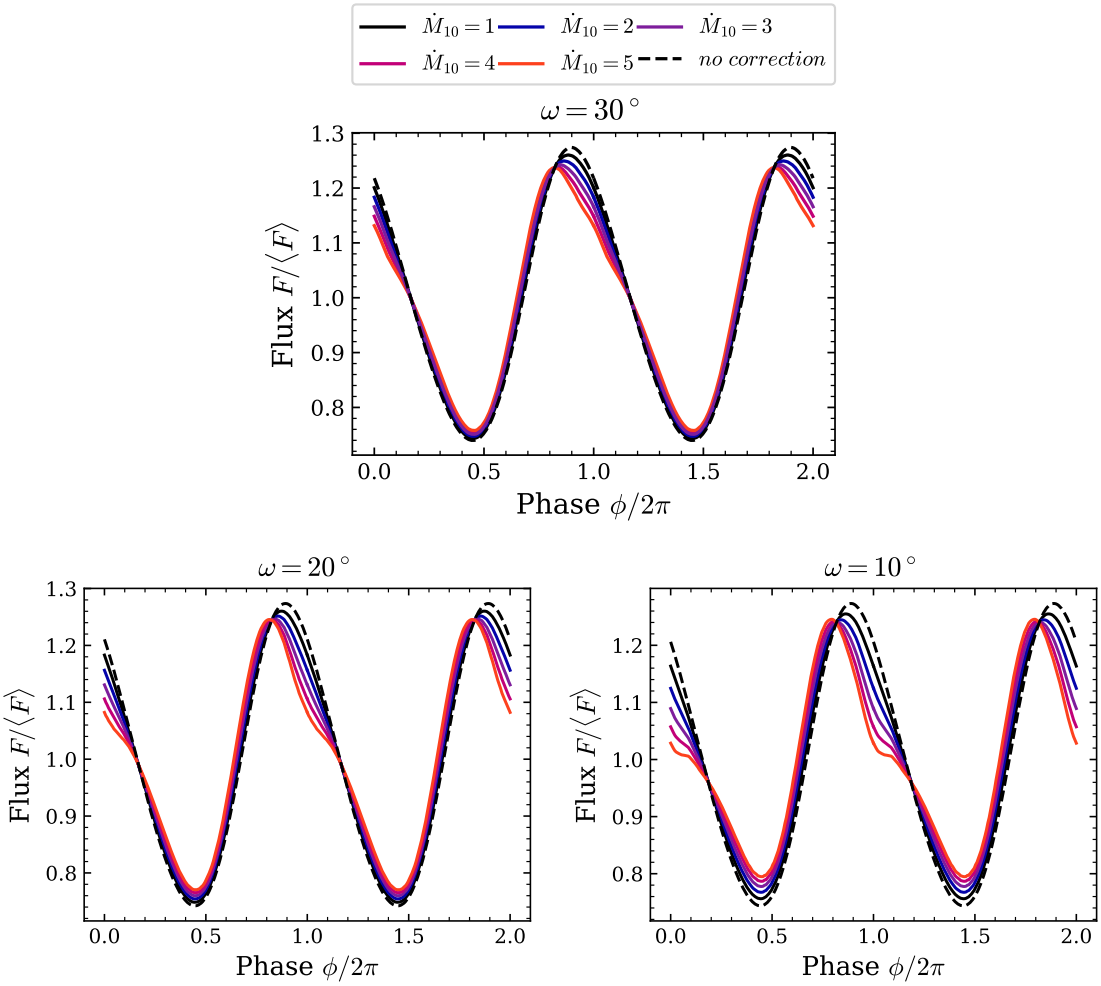

Figure 10: Pulse profiles using the optical depth correction model at different accretion rates and hot spot radii at an energy of 10 keV. Note that the flux is relative, the actual corrected profiles have lower flux overall. The observer inclination is $i = 60°$, and the spot colatitude is $\theta_0 = 20°$.

similar, which might cause fit degeneracies for the two parameters. For small θ_0, the Doppler boosting and aberration warping the pulse profile are weaker, and the dip is closer to the flux maximum. A large i angle has a similar effect, but the dip tends to be much more shallow. The depth of the dip appears to be the strongest when both θ_0 and i are small, in the most extreme case it is even deeper than the pulse minimum.

The optical depth correction has little effect on a secondary antipodal spot, because it is significantly further away from the observer than the primary spot and therefore the optical depth remains nearly constant. For this reason I did not include plots of such here. However, the correction should be applied to both spots as the optical depth is still nonzero.

To test this model, I roughly compared simulated profiles to measured pulse profiles of accretion powered millisecond pulsar SAX J1808.4−3658. The inclination of the neutron star has been previously measured to be roughly around $i \sim 60°$, and

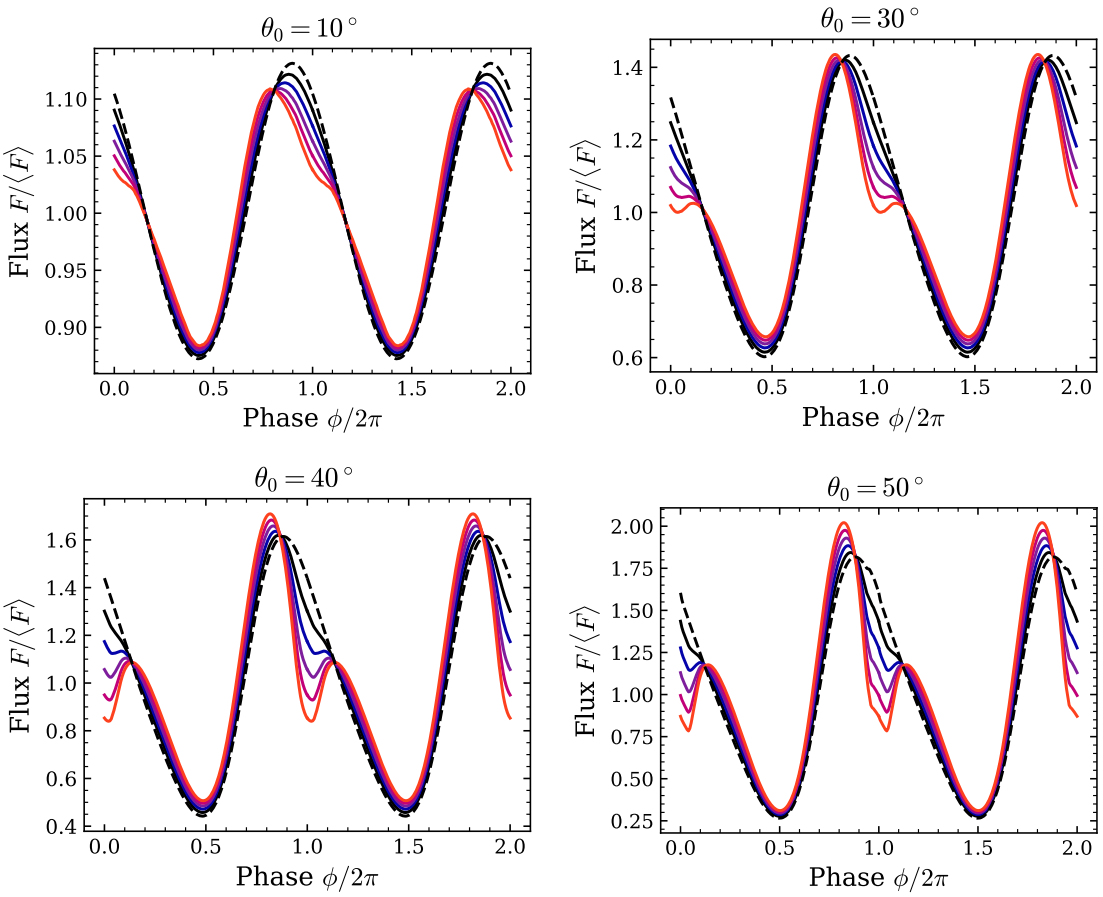

Figure 11: Pulse profiles using the optical depth correction model at different accretion rates and spot colatitudes at an energy of 10 keV. The observer inclination is $i = 60°$, and the spot radius is $\omega = 15°$. The accretion rates follow the same colours as figure 10.

the spot colatitude is estimated to be $\theta_0 \sim 10°$. During the peak of its 2002 outburst, the pulse had a very noticeable secondary minimum [66]. For the comparison, I used a singular spot with $i = 58.3°$, $\theta_0 = 3.7°$, $\omega = 30°$, and $\dot{M}_{10} = 3.5$ at an energy of 10 keV. While it is not an optimized fit, the shape of the dip is quite similar to observations.

Finding a comparable profile for the slow decay portion of the same burst was more challenging. The most similar profile profile I was able to find included an antipodal spot and used the parameters $i = 58.3°$, $\theta_0 = 6.1°$, $\omega = 15°$, and $\dot{M}_{10} = 2.5$, again at an energy of 10 keV. The shape of the pulse is once again quite similar, but the dip was much too shallow. Models with an antipodal spot and a higher θ_0 appear to represent this profile better, which might indicate a change in accretion geometry. Further study of these profiles is necessary to analyze this further. Both of the simulated profiles are presented alongside the observed profiles in figure 13.

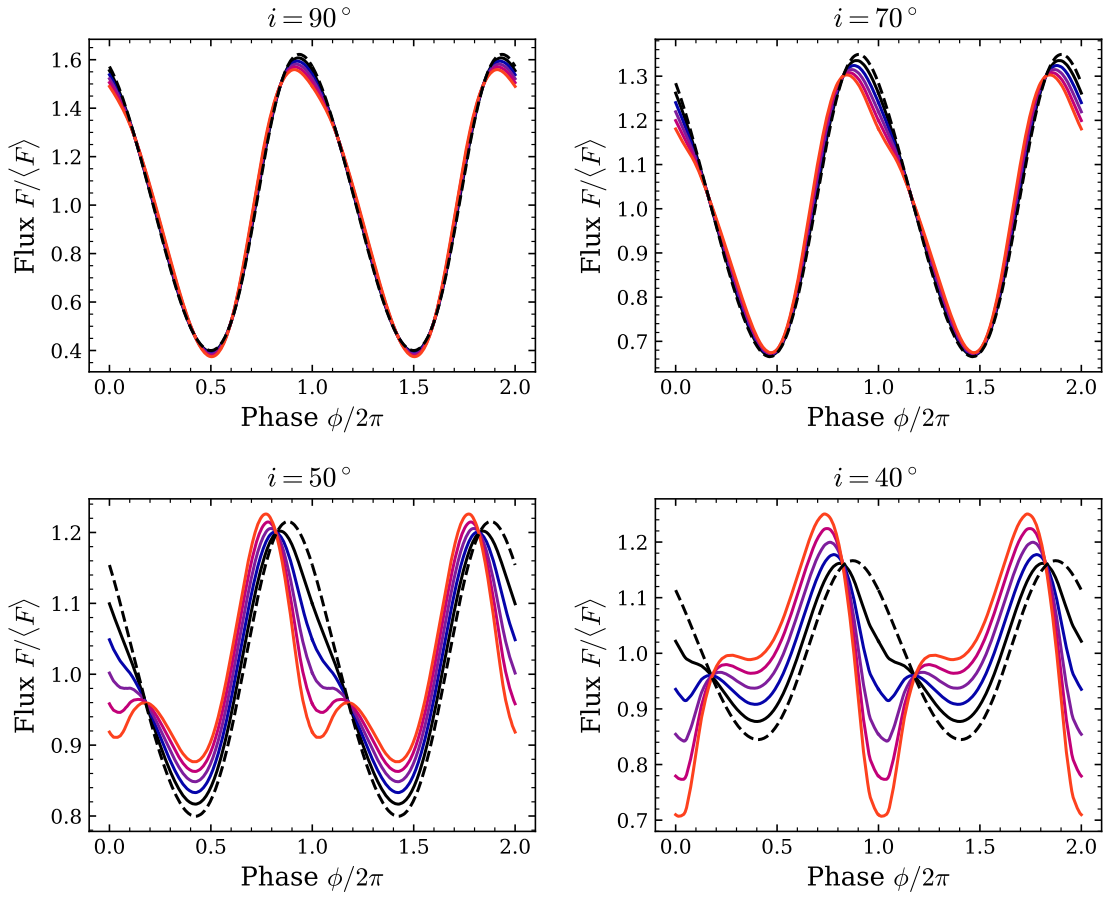

Figure 12: Pulse profiles using the optical depth correction model at different accretion rates and observer inclinations at an energy of 10 keV. The spot colatitude is $\theta_0 = 20°$, and the spot radius is $\omega = 15°$. The accretion rates follow the same colours as figure 10.

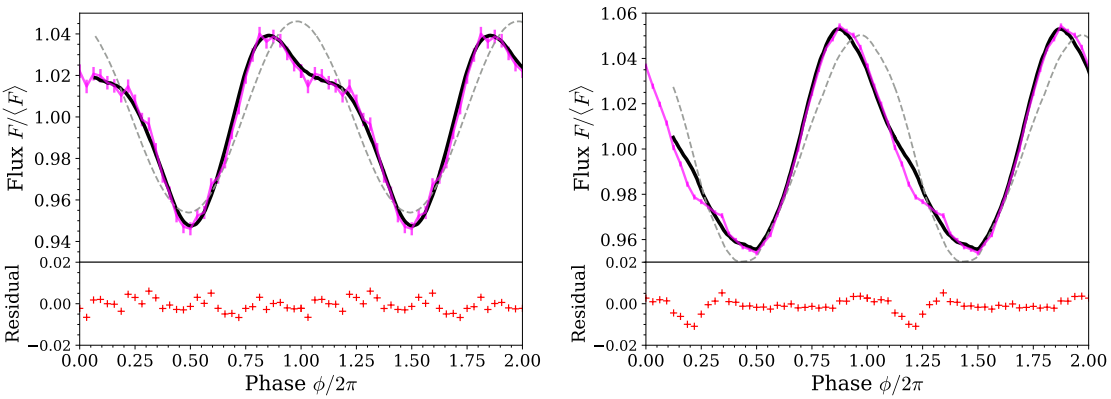

Figure 13: The pulse profile of SAX J1808.4−3658 during its outburst peak (left) and slow decay phase (right) compared to the simulated pulse profiles with the optical depth correction. The grey dashed line represents the uncorrected profile.

5 Summary

The most stringent constraints on the cold dense matter EoS have been achieved through measuring the maximum mass and tidal deformability of neutron stars, but the number of viable models is still huge. To achieve better accuracy, further measurements are needed. Probing the EoS through X-ray observations is a challenging task due to the many systematic factors involved, but it shows promise. Spectral fitting in particular has many issues regarding distance and the emission spectrum. The cooling tail method can bypass the problem with distance through measuring the Eddington temperature. The method has good potential for accurate $M - R$ measurement, but has yet to provide strong mass constraints [60]. There are several other possible methods such as QPO modeling, but none of them have been utilized in practice yet.

Besides the cooling tail method, so far the most reliable $M - R$ measurements have been achieved with pulse profile modeling. Pulse profile modeling still faces challenges in its model parameters that can be difficult to determine and degenerate with each other. Phase resolved polarization measurement through instruments such as *IXPE* would aid with resolving the geometric parameters in the future [54]. *NICER* has been shown to be capable of achieving good measurement accuracy with rotation powered millisecond pulsars, however the analyses of the currently available data are not in consensus about the results [61, 62]. Further study of the emission mechanism might be necessary to achieve more reliable constraints [52].

The optical depth of the accretion flow in disk accreting neutron stars can cause a significant secondary minimum in the pulse profile. The simplified model presented here is capable of recreating the effect with realistic parameters. The main model parameters are the observer inclination, the spot colatitude, the spot size, and the accretion rate. The accretion rate can be estimated with the accretion luminosity, which cannot be measured all that accurately due to its dependence on distance. The spot size has previously been very difficult to constrain due to its weak effect on the pulse profile, but it is a major factor in this model. As the depth and location of the dip is sensitive to many model parameters, the correction model might potentially assist in measuring them more accurately. More rigorous statistical analysis of the optical depth correction would help ascertain its impact.

References

[1] Vladimir M. Lipunov. *Astrophysics of Neutron Stars*. Nauka, Moscow, 1992.

[2] Nathalie Degenaar and Valery F. Suleimanov. Testing the Equation of State with Electromagnetic Observations. In Luciano Rezzolla, Pierre Pizzochero, David Ian Jones, Nanda Rea, and Isaac Vidaña, editors, *Astrophysics and Space Science Library*, volume 457 of *Astrophysics and Space Science Library*, page 185, January 2018.

[3] Victoria M. Kaspi. Grand unification of neutron stars. *Proceedings of the National Academy of Science*, 107(16):7147–7152, April 2010.

[4] Sergio Campana and Tiziana Di Salvo. Accreting Pulsars: Mixing-up Accretion Phases in Transitional Systems. In Luciano Rezzolla, Pierre Pizzochero, David Ian Jones, Nanda Rea, and Isaac Vidaña, editors, *Astrophysics and Space Science Library*, volume 457 of *Astrophysics and Space Science Library*, page 149, January 2018.

[5] G. Fiorella Burgio and Anthea F. Fantina. Nuclear Equation of State for Compact Stars and Supernovae. In Luciano Rezzolla, Pierre Pizzochero, David Ian Jones, Nanda Rea, and Isaac Vidaña, editors, *Astrophysics and Space Science Library*, volume 457 of *Astrophysics and Space Science Library*, page 255, January 2018.

[6] David Blaschke and Nicolas Chamel. Phases of Dense Matter in Compact Stars. In Luciano Rezzolla, Pierre Pizzochero, David Ian Jones, Nanda Rea, and Isaac Vidaña, editors, *Astrophysics and Space Science Library*, volume 457 of *Astrophysics and Space Science Library*, page 337, January 2018.

[7] J. R. Oppenheimer and G. M. Volkoff. On Massive Neutron Cores. *Physical Review*, 55(4):374–381, February 1939.

[8] Feryal Özel and Paulo Freire. Masses, Radii, and the Equation of State of Neutron Stars. *Annual Review of Astronomy and Astrophysics*, 54:401–440, September 2016.

[9] D. R. Lorimer and M. Kramer. *Handbook of Pulsar Astronomy*, volume 4. Press syndicate of the university of Cambridge, 2004.

[10] James M. Lattimer. The Nuclear Equation of State and Neutron Star Masses. *Annual Review of Nuclear and Particle Science*, 62(1):485–515, November 2012.

[11] John Antoniadis, Paulo C. C. Freire, Norbert Wex, and et. al. A Massive Pulsar in a Compact Relativistic Binary. *Science*, 340(6131):448, April 2013.

[12] H. T. Cromartie, E. Fonseca, S. M. Ransom, and et. al. Relativistic Shapiro delay measurements of an extremely massive millisecond pulsar. *Nature Astronomy*, 4:72–76, January 2020.

[13] M. H. van Kerkwijk, R. P. Breton, and S. R. Kulkarni. Evidence for a Massive Neutron Star from a Radial-velocity Study of the Companion to the Black-widow Pulsar PSR B1957+20. *The Astrophysical Journal*, 728(2):95, February 2011.

[14] Roger W. Romani, Alexei V. Filippenko, Jeffrey M. Silverman, and et. al. PSR J1311-3430: A Heavyweight Neutron Star with a Flyweight Helium Companion. *The Astrophysical Journal Letters*, 760(2):L36, December 2012.

[15] P. Haensel, J. L. Zdunik, M. Bejger, and J. M. Lattimer. Keplerian frequency of uniformly rotating neutron stars and strange stars. *Astronomy & Astrophysics*, 502(2):605–610, August 2009.

[16] A. Watts, C. M. Espinoza, R. Xu, and et. al. Probing the neutron star interior and the Equation of State of cold dense matter with the SKA. In *Advancing Astrophysics with the Square Kilometre Array (AASKA14)*, page 43, April 2015.

[17] A. Patruno, B. Haskell, and N. Andersson. The Spin Distribution of Fast-spinning Neutron Stars in Low-mass X-Ray Binaries: Evidence for Two Sub-populations. *The Astrophysical Journal*, 850(1):106, November 2017.

[18] B. P. Abbott, R. Abbott, T. D. Abbott, and et. al. GW170817: Observation of Gravitational Waves from a Binary Neutron Star Inspiral. *Physical Review Letters*, 119(16):161101, October 2017.

[19] Andreas Guerra Chaves and Tanja Hinderer. Probing the equation of state of neutron star matter with gravitational waves from binary inspirals in light of GW170817: a brief review. *Journal of Physics G Nuclear Physics*, 46(12):123002, December 2019.

[20] Kentaro Takami, Luciano Rezzolla, and Luca Baiotti. Spectral properties of the post-merger gravitational-wave signal from binary neutron stars. *Physical Review D*, 91(6):064001, March 2015.

[21] Ryan J. Foley, David A. Coulter, Charles D. Kilpatrick, and et. al. Updated parameter estimates for GW190425 using astrophysical arguments and implications for the electromagnetic counterpart. *Monthly Notices of the Royal Astronomical Society*, 494(1):190–198, May 2020.

[22] Eemeli Annala, Tyler Gorda, Evangelia Katerini, and et. al. Multimessenger Constraints for Ultradense Matter. *Physical Review X*, 12(1):011058, January 2022.

[23] M. Coleman Miller. Astrophysical Constraints on Dense Matter in Neutron Stars. *arXiv e-prints*, page arXiv:1312.0029, November 2013.

[24] Michi Bauböck, Feryal Özel, Dimitrios Psaltis, and Sharon M. Morsink. Rotational Corrections to Neutron-star Radius Measurements from Thermal Spectra. *The Astrophysical Journal*, 799(1):22, January 2015.

[25] V. F. Suleimanov, J. Poutanen, D. Klochkov, and K. Werner. Measuring the basic parameters of neutron stars using model atmospheres. *European Physical Journal A*, 52:20, February 2016.

[26] V. E. Zavlin, G. G. Pavlov, and Yu. A. Shibanov. Model neutron star atmospheres with low magnetic fields. I. Atmospheres in radiative equilibrium. *Astronomy & Astrophysics*, 315:141–152, November 1996.

[27] Feryal Özel. Surface emission from neutron stars and implications for the physics of their interiors. *Reports on Progress in Physics*, 76(1):016901, January 2013.

[28] Feryal Özel and Dimitrios Psaltis. Spectral Lines from Rotating Neutron Stars. *The Astrophysical Journal Letters*, 582(1):L31–L34, January 2003.

[29] J. J. M. in 't Zand, T. Bagnoli, C. D'Angelo, and et. al. Chandra spectroscopy of Rapid Burster type-I X-ray bursts. *arXiv e-prints*, page arXiv:1703.07221, March 2017.

[30] Craig O. Heinke. Constraints on physics of neutron stars from X-ray observations. In *Journal of Physics Conference Series*, volume 432 of *Journal of Physics Conference Series*, page 012001, April 2013.

[31] Nathalie Degenaar, David R. Ballantyne, Tomaso Belloni, and et. al. Accretion Disks and Coronae in the X-Ray Flashlight. *Space Science Reviews*, 214(1):15, February 2018.

[32] J. Nättilä, A. W. Steiner, J. J. E. Kajava, and et. al. Equation of state constraints for the cold dense matter inside neutron stars using the cooling tail method. *Astronomy & Astrophysics*, 591:A25, June 2016.

[33] Feryal Özel, Tolga Güver, and Dimitrios Psaltis. The Mass and Radius of the Neutron Star in EXO 1745-248. *The Astrophysical Journal*, 693(2):1775–1779, March 2009.

[34] Andrew W. Steiner, James M. Lattimer, and Edward F. Brown. The Equation of State from Observed Masses and Radii of Neutron Stars. *The Astrophysical Journal*, 722(1):33–54, October 2010.

[35] Valery Suleimanov, Juri Poutanen, Mikhail Revnivtsev, and Klaus Werner. A Neutron Star Stiff Equation of State Derived from Cooling Phases of the X-Ray Burster 4U 1724-307. *The Astrophysical Journal*, 742(2):122, December 2011.

[36] V. Suleimanov, J. Poutanen, and K. Werner. X-ray bursting neutron star atmosphere models using an exact relativistic kinetic equation for Compton scattering. *Astronomy & Astrophysics*, 545:A120, September 2012.

[37] Nicolas Baillot d'Etivaux, Sebastien Guillot, Jérôme Margueron, and et. al. New Constraints on the Nuclear Equation of State from the Thermal Emission of Neutron Stars in Quiescent Low-mass X-Ray Binaries. *The Astrophysical Journal*, 887(1):48, December 2019.

[38] Slavko Bogdanov, Craig O. Heinke, Feryal Özel, and Tolga Güver. Neutron Star Mass-Radius Constraints of the Quiescent Low-mass X-Ray Binaries X7 and X5 in the Globular Cluster 47 Tuc. *The Astrophysical Journal*, 831(2):184, November 2016.

[39] Sebastien Guillot, Mathieu Servillat, Natalie A. Webb, and Robert E. Rutledge. Measurement of the Radius of Neutron Stars with High Signal-to-noise Quiescent Low-mass X-Ray Binaries in Globular Clusters. *The Astrophysical Journal*, 772(1):7, July 2013.

[40] Juri Poutanen and Marek Gierliński. On the nature of the X-ray emission from the accreting millisecond pulsar SAX J1808.4-3658. *Monthly Notices of the Royal Astronomical Society*, 343(4):1301–1311, August 2003.

[41] Juri Poutanen. Accurate analytic formula for light bending in Schwarzschild metric. *Astronomy & Astrophysics*, 640:A24, August 2020.

[42] Juri Poutanen and Andrei M. Beloborodov. Pulse profiles of millisecond pulsars and their Fourier amplitudes. *Monthly Notices of the Royal Astronomical Society*, 373(2):836–844, December 2006.

[43] Dimitrios Psaltis, Feryal Özel, and Deepto Chakrabarty. Prospects for Measuring Neutron-star Masses and Radii with X-Ray Pulse Profile Modeling. *The Astrophysical Journal*, 787(2):136, June 2014.

[44] Coire Cadeau, Sharon M. Morsink, Denis Leahy, and Sheldon S. Campbell. Light Curves for Rapidly Rotating Neutron Stars. *The Astrophysical Journal*, 654(1):458–469, January 2007.

[45] Valery F. Suleimanov, Juri Poutanen, and Klaus Werner. Observational appearance of rapidly rotating neutron stars. X-ray bursts, cooling tail method, and radius determination. *Astronomy & Astrophysics*, 639:A33, July 2020.

[46] Slavko Bogdanov, Frederick K. Lamb, Simin Mahmoodifar, and et. al. Constraining the Neutron Star Mass-Radius Relation and Dense Matter Equation of State with NICER. II. Emission from Hot Spots on a Rapidly Rotating Neutron Star. *The Astrophysical Journal Letters*, 887(1):L26, December 2019.

[47] Frederick K. Lamb, Stratos Boutloukos, Sandor Van Wassenhove, and et. al. Origin of Intermittent Accretion-Powered X-ray Oscillations in Neutron Stars with Millisecond Spin Periods. *The Astrophysical Journal Letters*, 705(1):L36–L39, November 2009.

[48] A. K. Kulkarni and M. M. Romanova. Analytical hotspot shapes and magnetospheric radius from 3D simulations of magnetospheric accretion. *Monthly Notices of the Royal Astronomical Society*, 433(4):3048–3061, August 2013.

[49] Anna L. Watts, Nils Andersson, Deepto Chakrabarty, and et. al. Colloquium: Measuring the neutron star equation of state using x-ray timing. *Reviews of Modern Physics*, 88(2):021001, April 2016.

[50] Anna L. Watts. Constraining the neutron star equation of state using pulse profile modeling. In *Xiamen-CUSTIPEN Workshop on the Equation of State of Dense Neutron-Rich Matter in the Era of Gravitational Wave Astronomy*, volume 2127 of *American Institute of Physics Conference Series*, page 020008, July 2019.

[51] Anna L. Watts. Thermonuclear burst oscillations and the dense matter equation of state. In P. Weltevrede, B. B. P. Perera, L. L. Preston, and S. Sanidas, editors, *Pulsar Astrophysics the Next Fifty Years*, volume 337, pages 209–212, August 2018.

[52] Tuomo Salmi, Valery F. Suleimanov, Joonas Nättilä, and Juri Poutanen. Magnetospheric return-current-heated atmospheres of rotation-powered millisecond pulsars. *Astronomy & Astrophysics*, 641:A15, September 2020.

[53] T. Salmi, J. Nättilä, and J. Poutanen. Bayesian parameter constraints for neutron star masses and radii using X-ray timing observations of accretion-powered millisecond pulsars. *Astronomy & Astrophysics*, 618:A161, October 2018.

[54] Tuomo Salmi, Vladislav Loktev, Karri Korsman, and et. al. Neutron star parameter constraints for accretion-powered millisecond pulsars from the simulated IXPE data. *Astronomy & Astrophysics*, 646:A23, February 2021.

[55] Feryal Özel, Dimitrios Psaltis, Zaven Arzoumanian, and et. al. Measuring Neutron Star Radii via Pulse Profile Modeling with NICER. *The Astrophysical Journal*, 832(1):92, November 2016.

[56] Feryal Özel and Dimitrios Psaltis. Reconstructing the neutron-star equation of state from astrophysical measurements. *Physical Review D*, 80(10):103003, November 2009.

[57] Andrea Maselli, George Pappas, Paolo Pani, and et. al. A New Method to Constrain Neutron Star Structure from Quasi-periodic Oscillations. *The Astrophysical Journal*, 899(2):139, August 2020.

[58] R. Turolla, S. Zane, and A. L. Watts. Magnetars: the physics behind observations. A review. *Reports on Progress in Physics*, 78(11):116901, November 2015.

[59] Slavko Bogdanov, Sebastien Guillot, Paul S. Ray, and et. al. Constraining the Neutron Star Mass-Radius Relation and Dense Matter Equation of State with NICER. I. The Millisecond Pulsar X-Ray Data Set. *The Astrophysical Journal Letters*, 887(1):L25, December 2019.

[60] J. Nättilä, M. C. Miller, A. W. Steiner, J. J. E. Kajava, V. F. Suleimanov, and J. Poutanen. Neutron star mass and radius measurements from atmospheric model fits to X-ray burst cooling tail spectra. *Astronomy & Astrophysics*, 608:A31, December 2017.

[61] M. C. Miller, F. K. Lamb, A. J. Dittmann, and et. al. PSR J0030+0451 Mass and Radius from NICER Data and Implications for the Properties of Neutron Star Matter. *The Astrophysical Journal Letters*, 887(1):L24, December 2019.

[62] T. E. Riley, A. L. Watts, S. Bogdanov, and et. al. A NICER View of PSR J0030+0451: Millisecond Pulsar Parameter Estimation. *The Astrophysical Journal Letters*, 887(1):L21, December 2019.

[63] A. V. Bilous, A. L. Watts, A. K. Harding, and et. al. A NICER View of PSR J0030+0451: Evidence for a Global-scale Multipolar Magnetic Field. *The Astrophysical Journal Letters*, 887(1):L23, December 2019.

[64] M. C. Miller, F. K. Lamb, A. J. Dittmann, and et. al. The Radius of PSR J0740+6620 from NICER and XMM-Newton Data. *The Astrophysical Journal Letters*, 918(2):L28, September 2021.

[65] Thomas E. Riley, Anna L. Watts, Paul S. Ray, and et. al. A NICER View of the Massive Pulsar PSR J0740+6620 Informed by Radio Timing and XMM-Newton Spectroscopy. *The Astrophysical Journal Letters*, 918(2):L27, September 2021.

[66] Askar Ibragimov and Juri Poutanen. Accreting millisecond pulsar SAX J1808.4-3658 during its 2002 outburst: evidence for a receding disc. *Monthly Notices of the Royal Astronomical Society*, 400(1):492–508, 11 2009.

[67] Alexander Mushtukov and Sergey Tsygankov. Accreting strongly magnetised neutron stars: X-ray Pulsars. *arXiv e-prints*, page arXiv:2204.14185, April 2022.

[68] Andrei M. Beloborodov. Gravitational Bending of Light Near Compact Objects. *The Astrophysical Journal Letters*, 566(2):L85–L88, February 2002.

[69] K. Viironen and J. Poutanen. Light curves and polarization of accretion- and nuclear-powered millisecond pulsars. *Astronomy & Astrophysics*, 426:985–997, November 2004.